Research Square

Preprints are preliminary reports that have not undergone peer review.
They should not be considered conclusive, used to inform clinical practice,
or referenced by the media as validated information.

Control of Density Down-Ramp Injection in a Segmented Capillary Gas Cell for Laser Wakefield Accelerators

Sihyeon Lee
Gwangju Institute of Science and Technology
Junyeong Jeong
Ulsan National Institute of Science and Technology
Minseok Kim
Pohang Accelerator Laboratory
Myunghoon Cho
Pohang Accelerator Laboratory
Seong-hoon Kwon
Pohang Accelerator Laboratory
Min Sup Hur
Ulsan National Institute of Science and Technology
Hyyong Suk
Gwangju Institute of Science and Technology
Inhyuk Nam
ihnam@unist.ac.kr

Ulsan National Institute of Science and Technology

Article

Keywords:

Posted Date: November 16th, 2026

DOI: https://doi.org/10.21203/rs.3.rs-11537823/v1

License: This work is licensed under a Creative Commons Attribution 4.0 International License.
Read Full License

Additional Declarations: No competing interests reported.

Control of Density Down-Ramp Injection in a Segmented Capillary Gas Cell for Laser Wakefield Accelerators

Sihyeon Lee[1], Junyeong Jeong[2], Minseok Kim[3], Myunghoon Cho[3], Seong-hoon Kwon[3], Min Sup Hur[2], Hyyong Suk[1,*] and Inhyuk Nam[2,*]

[1]Department of Physics and Photon Science, Gwangju Institute of Science and Technology, Gwangju 61005, South Korea
[2]Department of Physics, Ulsan National Institute of Science and Technology, Ulsan 44919, South Korea
[3]Pohang Accelerator Laboratory, POSTECH, Pohang 37673, South Korea

***Corresponding authors**:
Hyyong Suk (hysuk@gist.ac.kr); Inhyuk Nam (ihnam@unist.ac.kr)

Abstract

Laser wakefield acceleration (LWFA) can sustain accelerating fields of hundreds of GV/m, enabling compact sources of high-energy electron beams, ultrafast X-rays, and secondary particles. These applications require high-quality electron beams with stable and controllable properties. Here, we report controlled density down-ramp injection in a segmented capillary gas cell with independently supplied upstream and downstream sections. A narrow orifice between the modular capillary sections accelerates the gas flow through the constriction, creating a localized density down-ramp between two quasi-uniform plasma density plateaus. The tailored density profile localizes electron injection within the down-ramp while suppressing subsequent self-injection and the associated low-energy tail, thereby spatially separating the injection region from the subsequent acceleration region. We experimentally demonstrate a transition from self-injection to down-ramp injection, as evidenced by the suppression of the broad low-energy tail of the electron spectrum and the resulting dark-current-free electron beams. Under stable down-ramp injection conditions, the electron beams had an average peak energy of 350 MeV and an average relative energy spread of 7.6% (FWHM). Particle-in-cell (PIC) simulations are consistent with the experimental observations and show that electron injection is localized within the density down-ramp. These results establish the segmented capillary as a simple and flexible platform for tailoring longitudinal plasma density profiles and controlling electron

injection, enabling stable and controllable LWFA operation for a broad range of accelerator and radiation-source applications.

Introduction

Laser wakefield acceleration (LWFA) can sustain accelerating gradients of hundreds of GV/m, several orders of magnitude larger than those of conventional radio-frequency accelerators [1,2]. When an intense laser pulse is focused into an underdense plasma, its ponderomotive force expels the background electrons while the much heavier ions remain nearly at rest, forming an ion cavity that trails the pulse. In the strongly driven bubble (blowout) regime [3,4], electrons trapped at the back of the cavity can be accelerated to GeV energies over centimeter-scale distances. Since the first quasi-monoenergetic beams were reported [5–7], the energy reach has grown to the multi-GeV range in a 20-cm-long plasma waveguide [8], establishing LWFA as a route toward compact electron accelerators and bright femtosecond radiation sources [9].

LWFA beams are being developed as compact drivers for a range of applications, most of which require high-quality electron beams. They can drive compact free-electron lasers [10,11] or emit bright betatron X-rays that support high-resolution phase-contrast imaging of biological and material samples [12,13]. Directed onto high-Z targets, the beams can also generate compact secondary sources, including photoneutron sources [14], ultra-relativistic positrons for collider-related studies [15], and directional muon sources with potential applications in imaging large or shielded objects [16]. These applications require electron beams that are stable, reproducible, and tunable in energy with a small energy spread. Such beam quality is set mainly by the plasma source and by the process that injects electrons into the wakefield.

Controlling this injection process is therefore critical to LWFA, and several schemes have been demonstrated, including self-injection [3], ionization injection [17], and density down-ramp injection [18–28]. Among them, down-ramp injection is widely used because it localizes the trapping position, facilitating the generation of high-quality electron beams. In density down-ramp injection, the wake expands as the laser pulse propagates through the decreasing plasma density, reducing the wake phase velocity

and allowing electrons to be trapped within the density transition. This localized trapping separates injection from acceleration, allowing electrons trapped at the transition to utilize the available acceleration length downstream. Since the injection is confined to a short distance, the electrons experience similar acceleration lengths, which can contribute to a reduced energy spread. In addition, the plasma density behind the down-ramp is lower than that in the injection region, which extends the dephasing length and can therefore enable acceleration to higher energies.

Among the down-ramp schemes, blade-induced shocks in gas jets produce steep density transitions for controlled electron trapping [25]. Such a shock, however, also introduces a sharply rising upstream density profile. This profile can enhance relativistic self-focusing and thereby modify the laser evolution before injection. Electron trapping is sensitive to both the laser intensity and the wakefield evolution, so these modifications can affect the injection process. For optimization, a profile with flat plateaus on both sides of the down-ramp therefore provides more direct control over the injection conditions than a profile with a rising upstream section. Previous particle-in-cell (PIC) studies have shown that independent variation of the plateau density ratio and down-ramp length enables systematic control of electron beam charge, energy, energy spread, and emittance [22]. Several other approaches separate the injection from the subsequent acceleration. These include optically induced shock injection [26], tailored longitudinal density profiles that produce high-quality near-GeV beams and enable electron-energy tuning [27–29], multi-chamber gas targets that spatially localize ionization injection [30], and density-tapered capillary gas cells [31].

Along with controllability, long-term stability is another critical requirement for practical LWFA operation. Compared with open gas-jet targets, capillary gas cells can provide a more reproducible plasma environment and have demonstrated stable operation over extended periods, enabling high-statistics measurements and machine-learning-based optimization of LWFA [32,33]. Combining such operational stability with controlled down-ramp injection would therefore provide both reproducibility and tunability within a single plasma source. Down-ramp injection between two independently controlled density regions has been demonstrated using two separate gas sources in a gas-jet target [24]. However, to the best of our

knowledge, a capillary gas cell incorporating a localized internal down-ramp between independently controlled density plateaus has not yet been experimentally demonstrated.

In this work, we report controlled density down-ramp injection in a segmented capillary gas cell (SCG), in which a localized density down-ramp is formed between two quasi-uniform density plateaus. The SCG is assembled from modular sapphire blocks with drilled holes. A thin orifice-slit module between two of the blocks contains a narrow orifice that defines the density transition, while the sections on either side form the upstream and downstream plateaus. The two inlet pressures can be adjusted separately. By varying the downstream pressure while keeping the upstream pressure fixed, we observe a transition from self-injection to down-ramp injection. This transition is characterized by suppression of the broad low-energy tail, an increase in peak energy, and a reduction in energy spread. PIC simulations show that electron injection is localized near the density down-ramp, and an injection-threshold analysis indicates that the trapping condition is satisfied in the same region.

Results

Experimental setup

We employed an SCG incorporating a narrow orifice to control electron injection and suppress the low-energy tail associated with dark current. The LWFA experiments were conducted at the CoReLS (Center for Relativistic Laser Science) facility using a 150-TW Ti:sapphire laser system [34], with the experimental setup illustrated in Fig. 1(a). The laser parameters are given in Methods. The electron beam transverse profile and shot-to-shot pointing jitter were monitored using LANEX 1 positioned before the dipole magnet, while the energy spectrum was measured using a 1 T dipole magnet and two downstream LANEX screens (LANEX 2 and 3) with different spectral resolutions. The LANEX signals were imaged onto CCD cameras. The three screens were used together for electron beam energy calibration, in which the beam pointing measured on LANEX 1 was taken into account, improving the accuracy of the measurement.

Figure 1(b) shows a 3D model of the SCG, which consists of four sapphire modules with drilled holes. The first and fourth modules served as gas-inlet sections. The second module incorporated a 0.5-mm-diameter, 0.3-mm-long orifice. The third and fourth modules together formed the downstream acceleration section, with a combined on-axis length of 5 mm. The total on-axis channel length of the assembled SCG was 9.3 mm. Modules 1, 3, and 4 contained a 1-mm-diameter axial aperture, while the gas-inlet modules (1 and 4) additionally contained a 1.5-mm-diameter gas inlet.

The gas pressures at inlet-1 and inlet-2 are denoted by P_1 and P_2, respectively. When P_2 is lower than P_1, gas flows through the narrow orifice, where its expansion and acceleration produce a localized density down-ramp between two nearly uniform density plateaus. Figure 1(c) shows the pressure distribution in a longitudinal cross-section through the capillary axis for $P_1 = 220$ mbar and $P_2 = 150$ mbar. Figure 1(d) shows the longitudinal on-axis pressure profiles for $P_1 = 220$ mbar and $P_2 = 200, 150,$ and 100 mbar. The shaded gray region marks the longitudinal position of the orifice. As P_2 decreases, the pressure drop across the orifice becomes more pronounced, corresponding to a stronger density transition between the upstream and downstream sections. For the corresponding computational fluid dynamics (CFD) density profiles, the down-ramp length was defined as the distance over which the density decreased from 90% to 10% of the density interval between the density at the onset of the drop and that at the first downstream local minimum. Using this definition, the down-ramp lengths were approximately 260 μm, 300 μm, and 400 μm for $P_2 = 200, 150,$ and 100 mbar, respectively. Since the SCG has a circular aperture, in situ interferometric density measurements are difficult to perform. The formation of the density down-ramp around the orifice was therefore independently verified in a test capillary with the same orifice geometry using plasma-density measurements based on Stark broadening [35] (see Supplementary Information). Assuming complete ionization, the electron densities were estimated from the applied gas pressures using the pressure-to-density conversion described in our previous study [36].

Control of electron injection by the density down-ramp

To investigate the effect of the density down-ramp on electron injection, P_2 was varied while P_1 was kept fixed, and the resulting electron beam spectra were measured.

Figure 2 summarizes the measurements obtained near the transition between self-injection and down-ramp injection, allowing the change in electron beam characteristics across the transition threshold to be examined.

Figure 2(a) shows the electron beam spectra obtained while varying the estimated downstream electron density, with the upstream electron density fixed at approximately $6.2 \times 10^{18}\ \mathrm{cm}^{-3}$, corresponding to the fixed inlet-1 pressure of 220 mbar. The electron number densities were estimated from the backing pressures measured by digital gauges connected to the two gas inlets, taking into account the pressure loss in the gas delivery system, for which separate conversion factors were used for inlet-1 and inlet-2, and assuming full ionization of the gas. Within the gas-pressure resolution available in the present setup, a distinct transition in the electron beam spectra is observed over a downstream electron density interval of $(5.83–5.87) \times 10^{18}\ \mathrm{cm}^{-3}$, indicating that the transition threshold lies in this range. Above the threshold, the spectra are broad and contain pronounced low-energy tails characteristic of continuous self-injection. Below the threshold, the low-energy tails are strongly suppressed, while the peak energies increase markedly, consistent with down-ramp injection.

Figure 2(b) compares representative electron spectra from the self-injection and down-ramp injection regimes. The one-dimensional spectra were obtained by taking line profiles through the peak-signal positions in the LANEX 3 images, rather than by integrating the signal over the transverse direction. Compared with the self-injection case, the down-ramp injection spectrum exhibits a lower spectral intensity, a higher peak energy, and a substantially narrower energy spread. The strong suppression of the low-energy component is particularly evident in the down-ramp injection spectrum.

Figure 2(c) summarizes the relationship between the peak energy and the relative energy spread based on a total of 46 electron beam shots, including the 25 shots shown in Fig. 2(a). The relative FWHM energy spread was determined after correcting for the contribution of the transverse beam size, as described in Methods. The blue data points represent measurements obtained above the transition threshold and are therefore classified as self-injection, whereas the red data points represent measurements obtained below the transition threshold and are classified as down-ramp injection. Each point represents the mean value for shots obtained under the

corresponding density condition, and the horizontal and vertical error bars indicate the standard deviations of the peak energy and relative energy spread, respectively. A tendency toward a smaller relative energy spread at higher peak energy is observed, with the down-ramp injection data occupying the higher-energy and narrower-energy-spread region. This tendency is consistent with previous PIC simulation studies [21,22], which also reported that a larger injected charge can lead to a broader energy spread because of stronger beam loading.

Shots obtained just below the transition threshold often reached the highest electron energies. This behavior may reflect two effects. First, the relatively high downstream density close to the threshold may provide more favorable conditions for electron energy gain through the associated laser and wake evolution. Second, under these conditions, the smaller pressure difference across the orifice reduces both the density drop and the down-ramp length, which may reduce the spatial extent of the trapping region. This may reduce the number of trapped electrons, thereby reducing beam loading [37] and allowing the trapped electrons to gain more energy. Near the transition threshold, electron injection can be sensitive to small variations in both the plasma profile and laser evolution, including changes in the laser intensity or effective focal position [25,32]. To evaluate stable operation away from this transition, we selected a lower downstream density. However, when the downstream density was reduced below approximately $3.9 \times 10^{18}\ \mathrm{cm}^{-3}$, no electron beams were observed, indicating a lower density limit for reliable injection. Accordingly, a downstream density of $5.02 \times 10^{18}\ \mathrm{cm}^{-3}$, located between the transition threshold and the lower density limit, was selected for the stability measurement.

Figure 3 shows 52 consecutive electron beam shots obtained under this operating condition. The electron signals recorded simultaneously on LANEX 3, LANEX 2, and LANEX 1 are shown from top to bottom, demonstrating reproducible electron beam generation over the measurement sequence. To quantify the shot-to-shot behavior, Fig. 4 shows the one-dimensional LANEX 3 energy spectra obtained from these 52 shots. The dashed line represents the average spectrum, while the gray shaded region represents the 16th–84th percentile range of the spectral intensity at each energy, corresponding to the central 68% of the shot distribution. Over these 52 shots, the beam had an average peak energy of 350 MeV with an rms shot-to-shot fluctuation of

6.9%, an average relative FWHM energy spread of 7.6%, and an electron beam charge of approximately 0.2–1 pC.

PIC simulation results

PIC simulations were performed using the JoPIC code [38] to investigate the electron-injection dynamics under the experimental conditions. Two plasma density profiles were considered under identical laser conditions based on the experimental parameters described in Methods: a tailored density profile containing a localized down-ramp and a near-flat density profile for comparison. Figures 5(a) and 5(c) show the down-ramp and near-flat cases, respectively. Each panel shows the plasma electron density profile (n_e, black solid line), the peak normalized vector potential of the laser (a_0, magenta solid line), and a false-color map of the energy spectrum of electrons associated with the first wake period as a function of the propagation distance z. In both simulations, the laser undergoes self-focusing in the plasma, increasing a_0 and shifting the effective focal position upstream, toward the laser entrance, relative to the free-space focal position at $z = 5.9$ mm. The plasma density variation also affects the laser evolution; therefore, the injection dynamics in the down-ramp region should be interpreted by considering both the density variation and the accompanying evolution of the laser pulse and wakefield. As shown in Figs. 5(a) and 5(c), electron injection in the down-ramp case begins near the density transition at an earlier position along the propagation z-axis than in the near-flat case. This shift in the injection onset supports the interpretation that the density down-ramp induces electron injection rather than merely suppressing subsequent self-injection. Moreover, the injection remains localized in the down-ramp case, whereas continuous electron injection persists over a longer propagation distance in the near-flat case.

In the down-ramp case, the injected electrons reach their maximum energy at $\mathrm{z} = 7040\ \mu\mathrm{m}$, after which they enter a decelerating phase and their energy spectrum begins to broaden. Figure 5(b) shows the plasma density distribution (false-color map), the on-axis longitudinal electric field E_z (red line), and the accelerated electrons (green dots) at this propagation position as functions of the relative coordinate ($\zeta = z - ct$), where c is the speed of light in vacuum and t is the simulation time. The corresponding electron energy spectrum is also shown in green. At this maximum-

energy position, the trapped electrons are located near the center of the plasma bubble, where the longitudinal electric field is close to zero. In contrast, Fig. 5(d) shows that the near-flat case at the same propagation position contains substantially more injected electrons in the wakefield cavity as a result of continuous electron injection, with sufficiently strong beam loading to distort the bubble structure. In line with this behavior, the near-flat case exhibits a lower peak energy and a broader energy spectrum than the down-ramp case, consistent with the experimental trend. As the bunch in the down-ramp case propagates further into the decelerating phase, its energy spectrum continues to broaden. By the end of the simulation at $z = 12$ mm, the beam has a peak energy of 348 MeV, an rms energy spread of 1.7%, and a charge of 0.34 pC. These simulations show that the density down-ramp induces localized electron injection while suppressing continuous electron injection.

Injection-threshold analysis

To assess whether the electron injection observed in the PIC simulation is consistent with trapping induced by the density down-ramp, we applied the electron-trapping criterion proposed by Kostyukov et al. [39]:

$$3.8\gamma_0 < R^2F^2 \qquad (1)$$

where $R = r_b\omega_p/c$ is the normalized bubble radius, r_b is the physical bubble radius, F is the normalized electric-field parameter of the plasma cavity, and γ_0 is the Lorentz factor associated with the velocity of the bubble rear. Here, $\omega_p = \sqrt{n_e e^2/m_e\epsilon_0}$ is the plasma frequency, where $n_e$is the electron density, e is the elementary charge, m_e is the electron mass, and ϵ_0 is the vacuum permittivity.

For an expanding bubble, we use $\gamma_0 \simeq [2(dr_b/dt)/c]^{-1/2}$, together with $r_b \simeq 2\sqrt{a_0}c/\omega_p$ and $F = (a_0^2/2)/\sqrt{1 + a_0^2/2}$ [40]. Substituting these relations into equation (1) gives

$$\frac{1}{c}\frac{dr_b}{dt} > 7.22\frac{(1 + a_0^2/2)^2}{a_0^{10}}. \qquad (2)$$

We define the threshold ratio as the ratio of the left-hand side to the right-hand side of equation (2), such that electron trapping is expected when the ratio exceeds unity.

The threshold ratio was evaluated using the plasma density and laser amplitude obtained directly from the PIC simulation shown in Fig. 5(a). As shown in Fig. 6, the horizontal dotted line marks the trapping threshold at a ratio of 1, and the threshold ratio exceeds unity in the range $z \simeq$ 4.93–5.20 mm. In this region, the combined evolution of the plasma density and laser amplitude leads to bubble expansion, reducing the effective velocity of the bubble rear and facilitating electron trapping. The predicted trapping region closely overlaps with the region where electron injection begins in Fig. 5(a), supporting the interpretation that the injection is induced by the density down-ramp rather than merely resulting from the suppression of self-injection.

Discussion

The transition from self-injection to down-ramp injection can be controlled by reducing the downstream plasma density. At high downstream density, continuous self-injection generates a broad low-energy tail. As the downstream density is lowered below the transition threshold, this continuous injection is suppressed while localized trapping at the density down-ramp remains. When the downstream density was reduced further, electron beams were no longer observed. Therefore, a downstream density between the transition threshold and the lower density limit was selected for the stability measurement. At this operating point, the upstream and downstream densities were approximately 6.2×10^{18} and 5.0×10^{18} cm^{-3}, respectively, and electron beams were reproducibly generated over 52 consecutive shots. This reproducible operation demonstrates the robustness of the segmented-capillary down-ramp injection scheme.

Within the down-ramp injection regime, the highest electron energies were obtained close to the transition threshold. The PIC simulations further show that the density transition modifies the subsequent laser evolution; in Fig. 5(a), a_0 decreases rapidly after the down-ramp, which may weaken the wakefield and reduce the subsequent energy gain [21]. Together with possible variations in beam loading [22,37], these results indicate that both the density profile and the associated laser and wake evolution are important in determining the final beam energy.

The modular design of the segmented capillary provides flexibility for extending this injection scheme to different LWFA conditions. The quasi-uniform upstream plateau

allows the laser evolution before injection to be considered when selecting the orifice position, while the downstream density and section length provide additional control over the subsequent acceleration. The capillary and orifice dimensions can be scaled together to maintain a similar density-transition geometry under different laser and plasma conditions. This provides a route to combining localized down-ramp injection with capillary-discharge guiding, potentially enabling electron trapping at lower density and acceleration of the injected bunch over a longer guided distance to higher energies. The segmented capillary therefore provides a flexible platform for controlled injection and subsequent acceleration in longer, guided LWFA stages.

Conclusion

We have demonstrated controlled density down-ramp injection in an SCG, in which a narrow orifice forms a localized density transition between two quasi-uniform plasma density plateaus. By varying the downstream density while maintaining a fixed upstream density, we observed a transition from self-injection to down-ramp injection, accompanied by strong suppression of the broad low-energy component, an increase in the peak energy, and a reduction in the energy spread. At the selected down-ramp injection operating point, 52 consecutive shots yielded an average peak energy of 350 MeV, an average relative FWHM energy spread of 7.6%, and an rms shot-to-shot peak-energy fluctuation of 6.9%. PIC simulations showed that electron injection was localized near the density down-ramp, while the injection-threshold analysis predicted a trapping region that closely overlapped with the injection-onset region observed in the simulation. These results support the interpretation that the density down-ramp induces localized electron trapping through the coupled evolution of the plasma density, laser pulse, and wakefield. This segmented capillary configuration therefore provides a flexible platform for controlling electron injection and subsequent acceleration, with potential extension to discharge-guided configurations for higher-energy electron acceleration and radiation-source applications.

Methods

Segmented capillary gas cell

The SCG was assembled from four modular blocks, each machined from a $25\ \mathrm{mm} \times 25\ \mathrm{mm}$ square sapphire plate. The first and fourth blocks, located at the laser entrance and exit sides, respectively, were identical and each contained a 1-mm-diameter, 4-mm-long axial aperture and a gas-inlet port. The second block contained a 0.5-mm-diameter, 0.3-mm-long axial aperture, forming the narrow orifice slit between the two main capillary sections. The third block contained a 1-mm-diameter, 1-mm-long axial aperture. Helium was supplied independently through the two gas inlets using two mass-flow controllers (MFCs). The helium flow rates were adjusted independently to establish the desired inlet pressures P_1 and P_2, thereby controlling the gas densities on both sides of the narrow orifice slit.

Laser system

The experiments used a 150-TW-class Ti:sapphire laser system [34] at the CoReLS facility. The laser pulse energy before compression was 4.0–4.3 J, and the compressed pulse duration was approximately 25 fs (FWHM), with a full $1/e^2$ intensity width of approximately 40 fs. The overall energy transmission from before the compressor to the target plane was approximately 56%, with a compressor transmission of approximately 67%. A spherical mirror with a focal length of 1500 mm focused the laser beam, and a deformable mirror was used to optimize the wavefront at focus. The laser focus was positioned inside the SCG, and its longitudinal position was optimized experimentally. The focal spot diameters at the $1/e^2$ intensity level were 36 μm horizontally and 29 μm vertically. Approximately 59% of the on-target laser energy was contained within the focal spot. After accounting for these factors, the intensity averaged over the $1/e^2$ focal-spot area and the $1/e^2$ pulse duration was approximately $3.96-4.26 \times 10^{18}\ \mathrm{W/cm^2}$, corresponding to an effective normalized vector potential of $a_0 = 1.36$–1.41.

Electron spectrometer

The electron beam diagnostics consisted of three LANEX screens (LANEX 1–3) and a dipole magnet, as shown in Fig. 1. LANEX 1 was positioned 34.1 cm downstream of the capillary exit to record the undispersed electron beam profile, and the entrance of the dipole magnet was located 10 cm downstream of LANEX 1. The magnet had a magnetic field strength of 0.998 T and a magnetic length of 20 cm. LANEX 2 was placed directly at the magnet exit, whereas LANEX 3 was positioned 53.5 cm downstream of the magnet exit. The electron energy spectra were measured using the dispersed signals recorded on LANEX 2 and LANEX 3. The LANEX 2 and LANEX 3 signals were imaged using a CCD (pco.pixelfly) and an EMCCD (Andor iXon Ultra), respectively. The LANEX 1 imaging system had a calibrated angular scale of approximately 0.1 mrad per pixel. At an electron energy of 300 MeV, the corresponding energy resolutions were approximately $+3.75/-3.65$ MeV for LANEX 2 and ± 0.74 MeV for LANEX 3.

Charge calibration

The electron beam charge was calibrated using an imaging plate (IP, Fujifilm BAS-TR) positioned at the LANEX 3 location. The signal recorded on the IP was scanned by an IP reader (Fuji FLA7000) and converted to electron charge based on the corresponding calibration factor. The calibrated charge was then compared with the corresponding electron signal measured on LANEX 2 to establish a conversion between the LANEX 2 signal and the electron beam charge. Because the fading of the IP signal between exposure and readout was not taken into account, the measured charge is expected to be lower than the actual electron beam charge.

Correction for the transverse beam size

The measured energy spectrum is broadened not only by the intrinsic energy spread of the electron beam but also by the finite transverse beam size resulting from beam divergence. To account for this contribution, the transverse beam size on LANEX 3 was measured in the direction unaffected by the magnetic field. Assuming an

approximately circular electron beam profile, we used this width to estimate the contribution of the transverse beam size to the measured width in the energy-dispersive direction. Let $W_{\perp}$ denote the FWHM beam size measured in the non-dispersive direction and W_{disp} the FWHM measured in the energy-dispersive direction. The width associated with the energy dispersion was estimated by quadrature subtraction as $W_{corr}^2 = W_{disp}^2 - W_{\perp}^2$. Using the position of the peak intensity as the center, the corrected spatial width W_{corr} was converted to an energy interval through the calibrated position-to-energy relation of the magnetic spectrometer. The resulting energy width, δE, was then used to define the relative energy spread as $\delta E/E_{peak}$, where E_{peak} is the electron energy corresponding to the peak of the measured spectrum.

CFD simulations

Three-dimensional CFD simulations were performed using ANSYS Fluent to characterize the gas density profile in the SCG. The steady-state helium flow through the capillary was modeled using a density-based solver with the SST k–ω turbulence model. The helium properties were described using the Peng–Robinson real-gas equation of state at a temperature of 300 K. Pressure-inlet boundary conditions were applied at the two gas inlets according to the experimental pressure settings, while the capillary exits were treated as pressure outlets representing vacuum conditions. The computational mesh contained 71,382 nodes and 283,628 elements, with a minimum mesh size of approximately 0.01 mm near the orifice. An implicit formulation with the Roe-FDS flux scheme and a Green–Gauss node-based gradient method was used. The Courant number was set to 0.5. The simulations were performed for various inlet-pressure conditions to obtain the three-dimensional gas density distribution and the corresponding longitudinal density profiles along the capillary axis.

PIC simulations

The PIC simulations were performed using the JoPIC code [38] in a quasi-three-dimensional cylindrical geometry. The electromagnetic fields were Fourier-expanded

in the azimuthal direction using a split-field approach. The laser propagated along the z-axis, with r denoting the radial coordinate. The grid spacings were $\Delta z = 32\ \mathrm{nm}$ and $\Delta r = 320\ \mathrm{nm}$. Each cell was initialized with $N_z \times N_r = 4 \times 12$ macroparticles, and two azimuthal modes were used. The plasma was initialized as fully ionized, with the ions represented as a stationary neutralizing background. The laser was modeled as a Gaussian beam with a central wavelength of 800 nm, a pulse duration of 40 fs at the $1/e^2$ intensity width, and a normalized vector potential of $a_0 = 1.4$. The laser was linearly polarized, with a beam waist of $18\ \mu\mathrm{m}$ and a focal position of $z = 5.9\ \mathrm{mm}$. The longitudinal plasma-density profiles were obtained from the CFD simulations. For the near-flat profile, the upstream and downstream electron densities were $n_{e,1} = 6.2 \times 10^{24}\ \mathrm{m^{-3}}$ ($\mathrm{P_1} = 220$ mbar) and $n_{e,2} = 5.9 \times 10^{24}\ \mathrm{m^{-3}}$ ($\mathrm{P_2} = 210$ mbar), while for the down-ramp profile, the corresponding densities were $n_{e,1} = 6.2 \times 10^{24}\ \mathrm{m^{-3}}$ ($\mathrm{P_1} = 220$ mbar) and $n_{e,2} = 4.2 \times 10^{24}\ \mathrm{m^{-3}}$ ($\mathrm{P_2} = 150$ mbar), respectively.

Data availability

The data that support the findings of this study are available from the corresponding author upon reasonable request.

Code availability

The JoPIC code used in this study is publicly available at https://github.com/scienter/jopic.

Acknowledgements

This work was supported by the National Research Foundation of Korea (Grant Nos. RS-2025-24873264 and RS-2022-NR070321), the Institute for Basic Science (IBS-R038-D1), and the InnoCORE program of the Ministry of Science and ICT (UNIST 1.260036.01). The authors acknowledge the CoReLS members who participated in laser operations.

Competing interests

The authors declare no competing interests.

Author contributions

S.L. and I.N. conceived the idea, designed the experiment, and analyzed the data. S.L., S.K., J.J., S.K., and I.N. performed the experiments. J.J. and S.L. performed the CFD simulations, and J.J. also prepared the plasma targets and measured the density profiles. M.K. contributed to the CFD simulations and the target design. S.L. performed the PIC simulations with assistance from M.C., and S.L. and M.H. contributed to the theoretical analysis. S.L. and I.N. wrote the manuscript with input from all authors. H.S. and I.N. supervised the project. All authors discussed the results and reviewed the manuscript.

References

1. Tajima, T. & Dawson, J. M. Laser electron accelerator. *Phys. Rev. Lett.* **43,** 267–270; 10.1103/PhysRevLett.43.267 (1979).
2. Esarey, E., Schroeder, C. B. & Leemans, W. P. Physics of laser-driven plasma-based electron accelerators. *Rev. Mod. Phys.* **81,** 1229–1285; 10.1103/RevModPhys.81.1229 (2009).
3. Pukhov, A. & Meyer-ter-Vehn, J. Laser wake field acceleration: the highly non-linear broken-wave regime. *Appl. Phys. B* **74,** 355–361; 10.1007/s003400200795 (2002).
4. Lu, W., Huang, C., Zhou, M., Mori, W. B. & Katsouleas, T. Nonlinear theory for relativistic plasma wakefields in the blowout regime. *Phys. Rev. Lett.* **96,** 165002; 10.1103/PhysRevLett.96.165002 (2006).
5. Geddes, C. G. R. et al. High-quality electron beams from a laser wakefield accelerator using plasma-channel guiding. *Nature* **431,** 538–541; 10.1038/nature02900 (2004).
6. Mangles, S. P. D. et al. Monoenergetic beams of relativistic electrons from intense laser–plasma interactions. *Nature* **431,** 535–538; 10.1038/nature02939 (2004).
7. Faure, J. et al. A laser–plasma accelerator producing monoenergetic electron beams. *Nature* **431,** 541–544; 10.1038/nature02963 (2004).
8. Gonsalves, A. J. et al. Petawatt laser guiding and electron beam acceleration to 8 GeV in a laser-heated capillary discharge waveguide. *Phys. Rev. Lett.* **122,** 084801; 10.1103/PhysRevLett.122.084801 (2019).
9. Albert, F. Principles and applications of x-ray light sources driven by laser wakefield acceleration. *Phys. Plasmas* **30,** 050902; 10.1063/5.0142033 (2023).
10. Wang, W. et al. Free-electron lasing at 27 nanometres based on a laser wakefield accelerator. *Nature* **595,** 516–520; 10.1038/s41586-021-03678-x (2021).
11. Labat, M. et al. Seeded free-electron laser driven by a compact laser plasma accelerator. *Nat. Photonics* **17,** 150–156; 10.1038/s41566-022-01104-w (2023).
12. Kneip, S. et al. X-ray phase contrast imaging of biological specimens with femtosecond pulses of betatron radiation from a compact laser plasma wakefield accelerator. *Appl. Phys. Lett.* **99,** 093701; 10.1063/1.3627216 (2011).
13. Wenz, J. et al. Quantitative X-ray phase-contrast microtomography from a compact laser-driven betatron source. *Nat. Commun.* **6,** 7568; 10.1038/ncomms8568 (2015).
14. Vallières, S. et al. High average-flux laser-driven neutron source. *Nat. Commun.* **16,** 11498; 10.1038/s41467-025-66535-9 (2025).
15. Streeter, M. J. V. et al. Narrow bandwidth, low-emittance positron beams from a laser-wakefield accelerator. *Sci. Rep.* **14,** 6001; 10.1038/s41598-024-56281-1 (2024).

16. Terzani, D. et al. Measurement of directional muon beams generated at the Berkeley Lab Laser Accelerator. *Phys. Rev. Accel. Beams* **28,** 103401; 10.1103/kxjr-h7zs (2025).
17. Pak, A. et al. Injection and trapping of tunnel-ionized electrons into laser-produced wakes. *Phys. Rev. Lett.* **104,** 025003; 10.1103/PhysRevLett.104.025003 (2010).
18. Bulanov, S. V., Naumova, N., Pegoraro, F. & Sakai, J. Particle injection into the wave acceleration phase due to nonlinear wake wave breaking. *Phys. Rev. E* **58,** R5257–R5260; 10.1103/PhysRevE.58.R5257 (1998).
19. Suk, H., Barov, N., Rosenzweig, J. B. & Esarey, E. Plasma electron trapping and acceleration in a plasma wake field using a density transition. *Phys. Rev. Lett.* **86,** 1011–1014; 10.1103/PhysRevLett.86.1011 (2001).
20. Brantov, A. V. et al. Controlled electron injection into the wake wave using plasma density inhomogeneity. *Phys. Plasmas* **15,** 073111; 10.1063/1.2956989 (2008).
21. Jain, A. et al. The effect of laser pulse evolution on down-ramp injection in laser wakefield accelerators. *Sci. Rep.* **14,** 19127; 10.1038/s41598-024-69049-4 (2024).
22. Ekerfelt, H. et al. A tunable electron beam source using trapping of electrons in a density down-ramp in laser wakefield acceleration. *Sci. Rep.* **7,** 12229; 10.1038/s41598-017-12560-8 (2017).
23. Geddes, C. G. R. et al. Plasma-density-gradient injection of low absolute-momentum-spread electron bunches. *Phys. Rev. Lett.* **100,** 215004; 10.1103/PhysRevLett.100.215004 (2008).
24. Hansson, M. et al. Down-ramp injection and independently controlled acceleration of electrons in a tailored laser wakefield accelerator. *Phys. Rev. ST Accel. Beams* **18,** 071303; 10.1103/PhysRevSTAB.18.071303 (2015).
25. Cobo, C. C. et al. Target sensitivity study of density transition-injected electrons in laser wakefield accelerators. *Phys. Rev. Accel. Beams* **27,** 111301; 10.1103/PhysRevAccelBeams.27.111301 (2024).
26. von Grafenstein, K. et al. Laser-accelerated electron beams at 1 GeV using optically-induced shock injection. *Sci. Rep.* **13,** 11680; 10.1038/s41598-023-38805-3 (2023).
27. Ke, L. T. et al. Near-GeV electron beams at a few per-mille level from a laser wakefield accelerator via density-tailored plasma. *Phys. Rev. Lett.* **126,** 214801; 10.1103/PhysRevLett.126.214801 (2021).
28. Gonsalves, A. J. et al. Tunable laser plasma accelerator based on longitudinal density tailoring. *Nat. Phys.* **7,** 862–866; 10.1038/nphys2071 (2011).
29. Gardner, C. & Dollar, F. Implementing Bayesian optimization to compare injection regimes and pulse propagation in two stage LWFA. New J. Phys. **27**, 124301; 10.1088/1367-2630/ae23f1 (2025).
30. Drobniak, P. et al. Two-chamber gas target for laser-plasma electron source. *Rev. Sci. Instrum.* **96,** 033304; 10.1063/5.0226055 (2025).

31. Kim, J. et al. Development of a density-tapered capillary gas cell for laser wakefield acceleration. *Rev. Sci. Instrum.* **92,** 023511; 10.1063/5.0009632 (2021).
32. Maier, A. R. et al. Decoding sources of energy variability in a laser-plasma accelerator. *Phys. Rev. X* **10,** 031039; 10.1103/PhysRevX.10.031039 (2020).
33. Jalas, S. et al. Bayesian optimization of a laser-plasma accelerator. Phys. Rev. Lett. **126**, 104801; 10.1103/PhysRevLett.126.104801 (2021).
34. Sung, J. H. et al. 5-Hz, 150-TW Ti:sapphire laser with high spatiotemporal quality. *J. Korean Phys. Soc.* **77,** 223–228; 10.3938/jkps.77.223 (2020).
35. Jang, D. G., Kim, M. S., Nam, I. H., Uhm, H. S. & Suk, H. Density evolution measurement of hydrogen plasma in capillary discharge by spectroscopy and interferometry methods. *Appl. Phys. Lett.* **99,** 141502; 10.1063/1.3643134 (2011).
36. Lee, S. et al. One-body capillary plasma source for plasma accelerator research at e-LABs. *Appl. Sci.* **13,** 2564; 10.3390/app13042564 (2023).
37. Rechatin, C. et al. Observation of beam loading in a laser-plasma accelerator. *Phys. Rev. Lett.* **103,** 194804; 10.1103/PhysRevLett.103.194804 (2009).
38. Cho, M., Kim, M. & Nam, I. Numerical dispersion free in longitudinal axis for particle-in-cell simulation. *J. Comput. Phys.* **462,** 111221; 10.1016/j.jcp.2022.111221 (2022).
39. Kostyukov, I., Nerush, E., Pukhov, A. & Seredov, V. A multidimensional theory for electron trapping by a plasma wake generated in the bubble regime. *New J. Phys.* **12,** 045009; 10.1088/1367-2630/12/4/045009 (2010).
40. Lu, W. et al. A nonlinear theory for multidimensional relativistic plasma wave wakefields. *Phys. Plasmas* **13,** 056709; 10.1063/1.2203364 (2006).

Figures

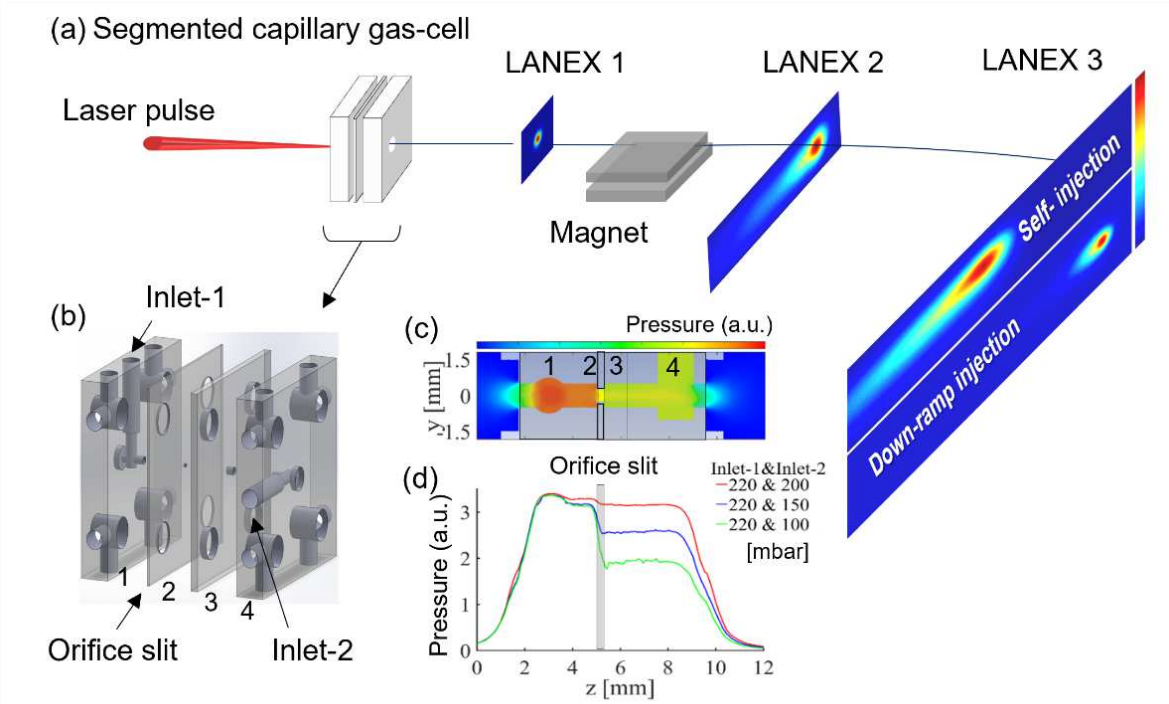


Figure 1. Experimental setup and the segmented capillary gas cell (SCG). (a) Experimental setup for LWFA using the SCG. LANEX 1, positioned before the dipole magnet, records the transverse electron beam profile, while LANEX 2 and LANEX 3 record the energy-dispersed electron beam signals. Representative LANEX 3 signals obtained in the self-injection and down-ramp injection regimes are also shown. (b) Three-dimensional model of the SCG assembled from four modular sapphire blocks (1–4). Inlet-1 and inlet-2 independently supply gas to the upstream and downstream sections, respectively, and the narrow orifice between the sections forms the localized density transition. (c) CFD-calculated gas pressure distribution in a longitudinal cross-section through the capillary axis for $P_1 = 220$ mbar and $P_2 = 150$ mbar. The positions labeled 1–4 correspond to the four modular capillary blocks shown in (b), and the position of the orifice is indicated. (d) Longitudinal on-axis pressure profiles for $P_1 = 220$ mbar and $P_2 = 200, 150,$ and 100 mbar. The gray shaded region indicates the longitudinal position of the orifice.

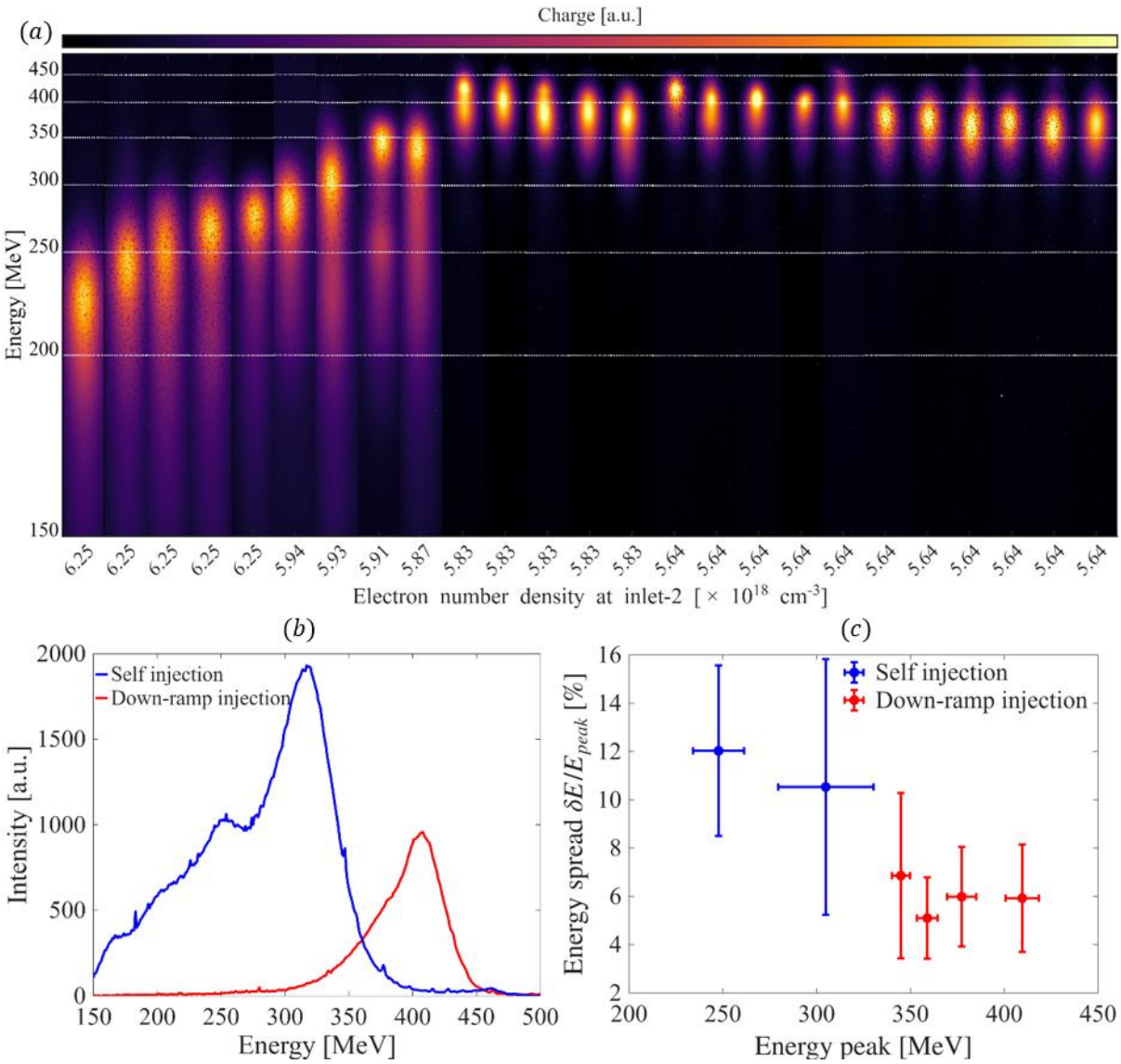


Figure 2. Electron spectra across the transition from self-injection to down-ramp injection. (a) Electron energy spectra obtained at a fixed upstream electron density of $6.2 \times 10^{18}\ \mathrm{cm}^{-3}$ for various downstream electron densities near the transition threshold. (b) Representative electron energy spectra in the self-injection (blue) and down-ramp injection (red) regimes. (c) Relative FWHM energy spread as a function of peak energy based on 46 electron beam shots, including the 25 shots shown in (a). Blue and red symbols represent the mean values for density conditions above and below the transition threshold, classified as self-injection and down-ramp injection, respectively. The horizontal and vertical error bars represent the standard deviations of the peak energy and relative FWHM energy spread, respectively.

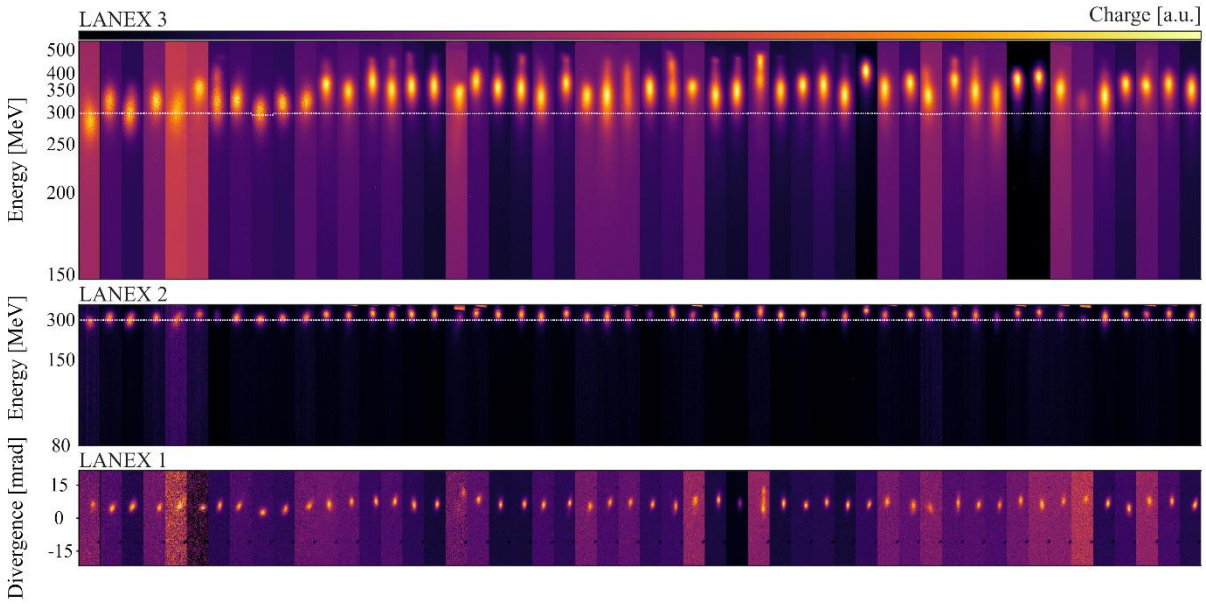


Figure 3. Electron beam signals from 52 consecutive shots in the down-ramp injection regime at an upstream electron density of $6.2 \times 10^{18}\ \mathrm{cm}^{-3}$ and a downstream electron density of $5.02 \times 10^{18}\ \mathrm{cm}^{-3}$. The signals recorded simultaneously on LANEX 3, LANEX 2, and LANEX 1 are shown from top to bottom, respectively. Each column corresponds to a single laser shot.

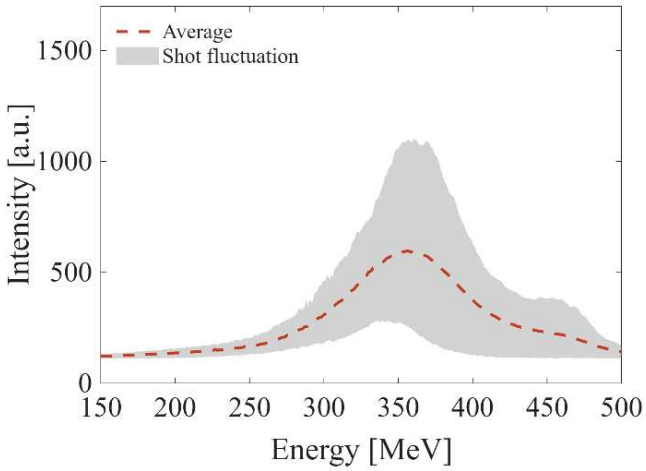


Figure 4. Statistical summary of the one-dimensional electron energy spectra extracted from line profiles through the peak-signal positions in the LANEX 3 images for 52 consecutive shots in the down-ramp injection regime at an upstream electron density of $6.2 \times 10^{18}\ \mathrm{cm}^{-3}$ and a downstream electron density of $5.02 \times 10^{18}\ \mathrm{cm}^{-3}$. The red dashed curve represents the mean spectrum, while the gray shaded region indicates the 16th–84th percentile range of the spectral intensity at each energy, corresponding to the central 68% of the shot distribution.

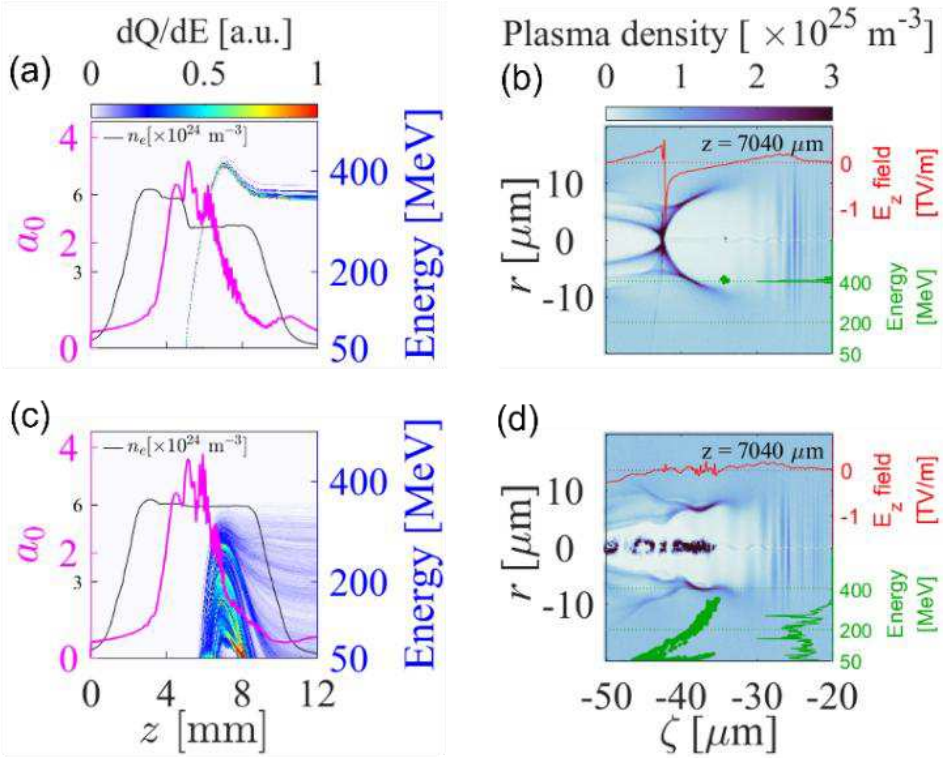


Figure 5. PIC simulation results. (a) Plasma electron density profile n_e (black line), peak normalized laser vector potential a_0 (magenta line), and a false-color map of the charge spectral density dQ/dE of electrons in the first wake period as functions of the propagation distance z for the down-ramp case. The electron energy corresponding to the false-color map is shown on the right vertical axis. (b) Snapshot at $z = 7040\ \mu\mathrm{m}$, corresponding to the position where the electron beam in (a) reaches its maximum energy, plotted in the co-moving coordinate $\zeta = z - ct$. The plasma electron density is shown as a false-color map, together with the on-axis longitudinal electric field E_z (red line), accelerated electrons (green dots), and the corresponding electron energy spectrum (green line). **(c)** Same quantities as in (a), but for a near-flat electron density profile. (d) Snapshot at $z = 7040\ \mu\mathrm{m}$, corresponding to (c). The maximum electron density in both cases is $n_{e,max} = 6.2 \times 10^{24}\ \mathrm{m}^{-3}$.

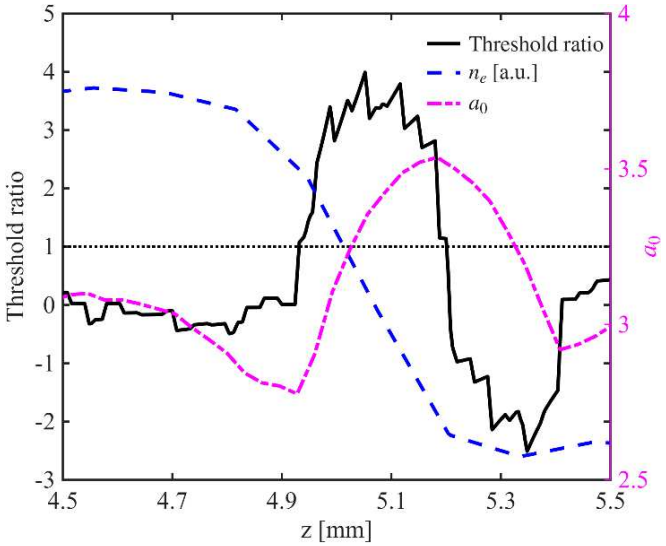


Figure 6. Injection-threshold analysis for the down-ramp case. The black solid line shows the threshold ratio, while the blue dashed and magenta dash-dotted lines represent the plasma electron density n_e (arbitrary units) and normalized laser amplitude a_0, respectively. The horizontal dotted line indicates the trapping threshold at a ratio of 1. Negative values of the threshold ratio correspond to regions where the bubble contracts rather than expands.

Supplementary Files

This is a list of supplementary files associated with this preprint. Click to download.

- SupplementaryInformation.docx